Annals of Biomedical Engineering, Vol. 44, No. 4, April 2016 *(© 2015)* pp. 993–1007
DOI: 10.1007/s10439-015-1417-1

On the Compressibility of Arterial Tissue

D. R. Nolan and J. P. McGarry

Biomedical Engineering, National University of Ireland, Galway, Ireland

(Received 22 April 2015; accepted 4 August 2015; published online 22 August 2015)

Associate Editor Estefanía Peña oversaw the review of this article.

Abstract—Arterial tissue is commonly assumed to be incompressible. While this assumption is convenient for both experimentalists and theorists, the compressibility of arterial tissue has not been rigorously investigated. In the current study we present an experimental-computational methodology to determine the compressibility of aortic tissue and we demonstrate that specimens excised from an ovine descending aorta are significantly compressible. Specimens are stretched in the radial direction in order to fully characterise the mechanical behaviour of the tissue ground matrix. Additionally biaxial testing is performed to fully characterise the anisotropic contribution of reinforcing fibres. Due to the complexity of the experimental tests, which entail non-uniform finite deformation of a non-linear anisotropic material, it is necessary to implement an inverse finite element analysis scheme to characterise the mechanical behaviour of the arterial tissue. Results reveal that ovine aortic tissue is highly compressible; an effective Poisson's ratio of 0.44 is determined for the ground matrix component of the tissue. It is also demonstrated that correct characterisation of material compressibility has important implications for the calibration of anisotropic fibre properties using biaxial tests. Finally it is demonstrated that correct treatment of material compressibility has significant implications for the accurate prediction of the stress state in an artery under *in vivo* type loading.

Keywords—Compressibility, Anisotropy, Hyperelasticity, Arterial tissue, Mechanical properties.

INTRODUCTION

Biological soft tissues are commonly assumed to be incompressible, such that material volume is conserved under all loading configurations and only isochoric deformation occurs.[17] This assumption has important consequences for the interpretation of experimental data and for the formulation of constitutive laws. Conservation of volume imposes the kinematic constraint that the determinant of the deformation gradient **F** must always equal unity. This lemma simplifies analysis of mechanical tests on tissues. For instance in interpreting biaxial stretching in the 1- and 2-directions the out-of-plane component of the deformation gradient of an incompressible material is trivially given as $F_{33} = 1/(F_{11}F_{22})$. The deformation gradient can then be used to calculate the Cauchy stress from the experimentally measured nominal/first Piola–Kirchhoff stress.

The incompressibility assumption also simplifies theoretical analysis of soft tissue, allowing for the formulation of constitutive laws based only on isochoric invariants and reducing the required number of material parameters.[21,32] Several soft tissues exhibit anisotropy due to the preferential alignment of collagen or elastin fibres (e.g. arteries,[10] cartilage,[20] annulus fibrosis,[11] tendons[43]). A common approach to the modelling of fibre reinforced anisotropic soft tissue is to assume incompressibility, and hence formulate the contributions of the isotropic matrix and fibres in terms of isochoric invariants.[18,19,21,32] Enforcement of material incompressibility (e.g. *via* a penalty method or a Lagrange multiplier used in conjunction with mixed/hybrid finite element formulations) is required in finite element (FE) implementations of such laws.

Despite the widespread assumption of material incompressibility, supporting experimental evidence has not yet been established for many types of soft tissue. In fact, several experimental studies suggest that cartilage is compressible.[29,36] Based on such experimental observations several authors have treated soft tissue as compressible, but incorrectly used isochoric based hyperelastic models. A recent study by Nolan *et al.*[28] highlights the significant errors and unphysical

---

Address correspondence to J. P. McGarry, Biomedical Engineering, National University of Ireland, Galway, Ireland. Electronic mail: patrick.mcgarry@nuigalway.ie

results that emerge when perfect material incompressibility is not enforced in an anisotropic hyperelastic formulation that is constructed using isochoric invariants.

Arterial tissue is one of the most widely studied soft tissues, both experimentally and computationally. Computational models of arteries generally assume incompressibility, with the experimental study of Carew *et al.*[4] frequently cited as support for this assumption. However, Carew *et al.* in fact report volume changes of arterial tissue due to lumen inflation and conclude that the material is slightly compressible, but may be regarded as incompressible at small strains. Other studies (performed three to six decades ago) suggest that arterial tissue may be considered to be slightly compressible.[6,24,41] Recent reviews of the literature[8,46] have critiqued techniques previously used to measure arterial compressibility and concluded that a contemporary study of the topic is warranted.

The current study presents a methodology to assess the compressibility of arterial tissue and parse the isotropic ground matrix and anisotropic fibre contributions. Cylindrical discs of ovine arterial tissue are stretched in tension in the radial material axis. The volume of the specimen is measured before and after stretch using an imaging technique. Additionally, confined compression experiments are performed in order to demonstrate material compressibility under a compressive loading mode. Next, a calibration of material constants for a compressible anisotropic hyperelastic constitutive law is performed using biaxial experimental test data. Finally, the influence of compressibilty on predictions of arterial compliance and wall stress is examined through the FE simulation of artery inflation under an increasing lumen pressure.

MATERIALS AND METHODS

Compressible Anisotropic Constitutive Model

The incompressible anisotropic hyperelastic constitutive model for collagen fibre reinforced soft tissues by Holzapfel *et al.*[19] (HGO model) is commonly used to simulate arterial tissue. In a recent paper Nolan *et al.*[28] demonstrate that significant errors and unphysical behaviour are computed if the incompressibility requirement is not correctly enforced for this formulation. To overcome this limitation Nolan *et al.*[28] present a modified anisotropic (MA) model, a modification of the HGO model for simulation of compressible soft tissue. Based on the HGO model, the strain energy potential is additively decomposed into isotropic and anisotropic parts reflecting the anatomical structure of soft tissues ($\Psi = \Psi_{\text{iso}} + \Psi_{\text{aniso}}$). The isotropic term is a neo–Hookean material representative of the ground matrix of the tissue, while the anisotropic term represents the reinforcing collagen fibres embedded in the ground matrix. Importantly, in the MA model total anisotropic invariants (I_i), rather than isochoric anisotropic invariants ($\bar{I}_i$), are used to describe fibre stretching so that both isochoric and volumetric deformations contribute to the anisotropic stress tensor. The anisotropic strain energy is given as $\Psi_{\text{aniso}} = \frac{k_1}{2k_2}\sum_{i=4,6}\exp\left\{[k_2(I_i-1)^2]-1\right\}$. The total Cauchy stress for the MA model is,

$$\sigma = \kappa(J-1)\mathbf{I} + \frac{\mu}{\mathbf{J}^{5/3}}\left(\mathbf{B} - \frac{\mathbf{1}}{\mathbf{3}}\mathbf{I_1}\mathbf{I}\right) + \frac{2k_1}{J}\sum_{i=4,6}(I_i-1)\exp\left[k_2(I_i-1)^2\right](\mathbf{a_i}\otimes\mathbf{a_i}), \tag{1}$$

where the first term on the right hand side represents the hydrostatic stress contribution due to volumetric deformation of the compressible ground matrix, the second term represents the deviatoric stress contribution due to isochoric deformation of the ground matrix, the third term represents the total (both hydrostatic and deviatoric) anisotropic fibre stress contribution. J is the determinant of the deformation gradient $\mathbf{F}$, $\mathbf{B} = \mathbf{F}\mathbf{F}^{\mathrm{T}}$ is the left Cauchy–Green deformation tensor and $\mathbf{C} = \mathbf{F}^{\mathrm{T}}\mathbf{F}$ is the right Cauchy–Green deformation tensor. The first invariant I_1 is the trace of $\mathbf{B}$, $\mathbf{I}$ is the identity tensor, I_i ($i = 4, 6$ when two fibre families are present) is the anisotropic invariant defined as $I_i = \mathbf{a_{0i}} \cdot (\mathbf{C}\mathbf{a_{0i}})$ where $\mathbf{a_{0i}}$ is a unit vector indicating the direction of fibre reinforcement and $\mathbf{a_i}$ is the same vector in the deformed configuration given by $\mathbf{a_i} = \mathbf{F}\mathbf{a_{0i}}$, k_1 and k_2 are material constants. The operator $\otimes$ is the dyadic product of vectors and results in a second order tensor.

If we assume that there are two families ($i = 4, 6$) of symmetric reinforcing fibres that are confined to the $\theta - z$ plane[19] then the unit vector $\mathbf{a_{0i}}$ may be defined be a single parameter, an angle β (see Fig. 2b) where $\mathbf{a}_{04} = [\cos(\beta)\ \sin(\beta) 0]^{\mathrm{T}}$ and $\mathbf{a}_{06} = [\cos(\beta) \quad -\sin(\beta) \quad 0]^{\mathrm{T}}$ In this case five material constants are required for the complete calibration of Eq. (1): two isotropic constants μ and κ, and three anisotropic constants k_1, k_2 and the fibre angle β.

Compressibility of Arterial Tissue

Tissue Preparation

The descending aorta is excised from six sheep sourced from a local abattoir (Brady's, Athenry, Ireland). The vessels are stored at −80 °C until required, at which point they are defrosted in phosphate buffer solution at 3 °C. Any excess connective tissue is carefully removed from the surface of the

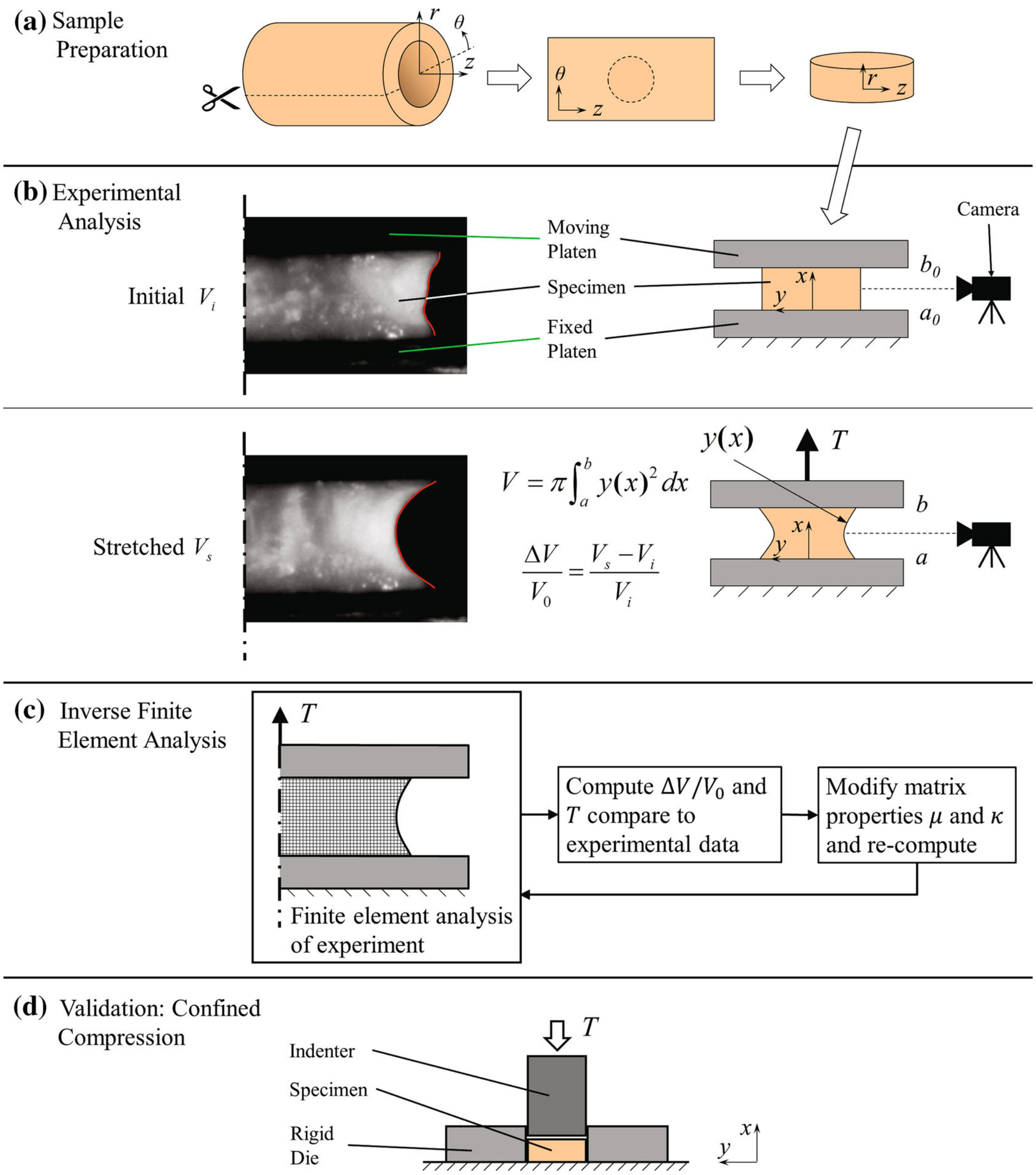

FIGURE 1. (a) Schematic outlining the specimen extraction. Tubular sections of arterial tissue from the descending aorta are cut along their axis to form planar sheets. A circular punch is used to cut cylindrical specimens from the planar sheet. (b) Schematic and images of the experiments performed to determine the compressibility of arterial tissue. Discs of arterial tissue are secured between two platens and an initial image is take to determine V_i the initial volume of the disc. The artery is subsequently stretched and a further image is taken to determine the stretched volume V_s along with the force measured by the load-cell at this stretch. (c) Flowchart outlining the inverse FE method used to determine the isotropic (ground matrix) material properties of arterial tissue. Assuming a neo–Hookean hyperelastic material, one may iteratively solve for the bulk modulus κ and shear modulus μ of the ground matrix. An axi-symmetric FE simulation of the above experiment is performed and the resultant force and volume change are computed and compared to the experimentally measured values. The values of κ and μ are iterated upon until a satisfactory match between the computational and experimental data is achieved. (d) Schematic outlining a confined compression experiment on cylindrical specimens of arterial tissue (identical to those in a)). A load is applied using a cylindrical indenter, specimens are not permitted to deform in the lateral direction. Confined compression results are used to validate μ and κ (determined in Fig. 1c).

tunica externa with a scissors and scalpel. The vessel is cut along its axis as shown in Fig. 1a and opened into a planar sheet. A circular punch with a diameter of 10 mm is used to cut out cylindrical disc specimens from this planar sheet for testing. The thickness of each specimen is measured with a micrometer. A total of 13 specimens are excised and tested.

Tensile Tests

Specimens are affixed between two platens using a cyanoacrylate adhesive (Loctite, Dusseldorf, Germany) (Fig. 1b). This assembly is then installed into a uniaxial mechanical testing machine (Zwick Z2.5, Ulm, Germany). The crosshead position of the machine is adjusted to ensure that the specimens are in a load free configuration at the start of the test. The specimens are then subjected to a tensile nominal stretch ratio $\lambda_{\text{nom}} = 1.28$ (where $\lambda_{\text{nom}} = (b - a)/(b_0 - a_0)$, see Fig. 1b) and then returned to their original state. This procedure is performed for two cycles. Force is recorded throughout the experiment and identical force–displacement curves for the two cycles indicate that the specimen has not been damaged, nor has it detached from the platen during the test. A camera system (1.31 MPx, 25 fps; uEye, IDS, Obersulm, Germany; videoXtens software, Zwick, Ulm, Germany) is set up to record the in-plane deformation of the cylindrical specimen as it is stretched. Images of the specimen are analysed in the initial state, and when fully stretched. These images are then used to compute volume change of the specimen during the test.

Volume Change Measurement

Images of the geometric profile of specimens are outlined using ImageJ[33] image processing software. The profiles are exported as a set of coordinates for 40 points on the free surface of the specimen. The radius of the specimen $y(x)$ is calculated at each of these 40 points (see Fig. 1b). To compute the specimen's volume the trapezoidal rule is used to evaluate the following integral:

$$V = \pi \int_a^b y(x)^2 \, dx, \tag{2}$$

where a is the x-position of the fixed platen and b is the x-position of the moving platen. Using this method, the initial specimen volume V_i and deformed specimen volume V_s are calculated. A second quasi-3D methodology for estimation of the volume change using two orthogonal camera projections of the deformed samples is presented in Appendix C. No statistically significant difference is calculated between the two methodologies of computing the sample volume change. The ratio of the volume change is given by $\Delta V/V_i = (V_s - V_i)/V_i$. If the tissue were truly incompressible then no volume change would be observed during the test. On the other hand, an observed volume change means that the material is compressible.

Calibration of Isotropic Ground Matrix

To further quantify the compressibility of arterial tissue, the above experiments are simulated using FE analysis. The MA model for compressible fibre reinforced soft tissue is presented in "Compressible Anisotropic Constitutive Model" section. It is generally assumed that fibres do not contribute to stress in compression (i.e. if $I_i < 1$ then $\Psi_{\text{aniso}} = 0$). In the above experiment, the specimen is stretched in the material's radial direction, causing a lateral contraction in the $\theta - z$ plane. Therefore a fibre contribution is not expected in this mode of applied loading. Rather, it is expected that the material stress and deformation is governed by the isotropic ground matrix, i.e. the first two terms of the right hand side of Eq. (1), characterised by the bulk modulus κ and the shear modulus μ. Even though the isotropic ground matrix is described by a hyperelastic material model, an effective material Poisson's ratio v_{eff} can be determined from the calibrated values of κ and μ, given in Eq. (3) as

$$v_{\text{eff}} = \frac{3\kappa/\mu - 2}{6\kappa/\mu + 2}. \tag{3}$$

Initial simulations are performed to established that the anisotropic fibre terms do not contribute to the material stress and deformation under the applied loading mode. Next, an inverse FE scheme is employed to calibrate κ and μ from the experimental data, as outlined in Fig. 1c. Briefly, trial bulk and shear moduli are set and an axisymmetric FE simulation of the experiment is performed. From this the resultant stretching force in the vertical direction (i.e. the force the load cell experiences) and the percentage change in volume are computed. The bulk and shear moduli are iterated upon until the experimentally measured stretching force and volume change are achieved.

All FE simulations are performed using Abaqus/Standard (v6.13-2, DS Simulia, RI, USA). Equation (1) is implemented in Abaqus *via* a user-defined Fortran subroutine (UMAT), for details of the consistent tangent matrix refer to Nolan *et al.*[28] The artery geometry in the undeformed reference configuration is constructed from experimental images taken before the load application (mean specimens geometric parameters for a range of tested samples, $n = 10$). A mesh sensitivity study reveals that a mesh consisting of 3000 four noded axisymmetric elements provides a converged solution. Mirroring the experimental set-up, the bottom face of the cylinder is fully constrained in the r, θ and z directions while the top face of the cylinder is displaced in the z direction to a nominal stretch of 1.28 whilst constrained in the r and θ directions.

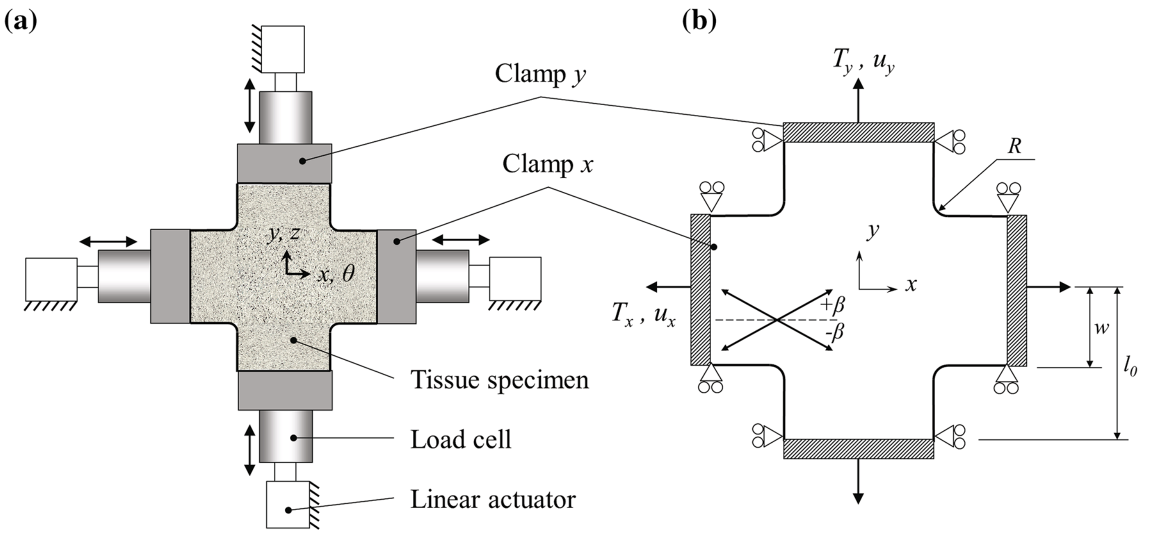

FIGURE 2. (a) Schematic of the biaxial experiment. A cruciform shaped tissue specimen is held rigidly in clamps. Each clamp is rigidly fixed to a load cell which in turn is rigidly fixed to a linear actuator controlling the displacement of the clamp. Force–displacement data are acquired in the x and y axes. Two displacement ratios, $u_x/u_y = 1$ and $u_x/u_y = 2$ are examined in the current study. (b) Schematic indicating the boundary conditions of the biaxial experiment outlined above in (a). In this setup, displacements are imposed at each of the clamps (u_x and u_y) and the resultant forces (F_x and F_y) are measured. The two families of reinforcing fibres are indicated at angles $\pm\beta$.

Confined Compression Tests

To further assess the compressibility of arterial tissue and validate the material parameters calculated for the ground matrix, a series of confined compression tests were performed on cylindrical specimens of arterial tissue ($n = 9$). Figure 1d outlines a schematic of the experiment. A specimen is placed into a rigid die, thus preventing any lateral deformation. Specimens are deformed by a cylindrical punch; axial nominal strains of 10% are applied. The experimental confined compression axial stress–strain relationship is then compared to predicted theoretical response using the compressible material properties determined from the tension tests described in the "Calibration of Isotropic Ground Matrix" section.

Biaxial Experiments

Biaxial stretch tests using cruciform specimens of arterial tissue are performed. An inverse FE method is used to interpret the biaxial tests and calibrate the constitutive model in Eq. (1).

Specimen Preparation

Specimens are excised from five ovine descending aortas using a custom made cruciform template. The geometry of the cruciforms are outlined in Fig. 2b. Cruciform arms are aligned with the axial and circumferential directions of the artery. Specimens have a half width $w_0 = 4$ mm, a half length $l_0 = 12$ mm, and a fillet radius $R = 3$ mm. The thickness of each specimen is measured using a micrometer. A total of six specimens are tested.

Biaxial Test Protocol

Figure 2a shows a schematic of the biaxial experimental set-up. The test apparatus consists of four fixed linear actuators which may be independently controlled. Each actuator houses a 100 N load cell which in turn is connected to the jaws. The jaws themselves have a roughened surface to prevent slippage during testing. Specimens are loaded into jaws with the circumferential direction θ aligned with the x-axis and the axial direction z with the y-axis of the machine (see Fig. 2b). Biaxial tests are performed on each of the specimens ($n = 6$) at a clamp displacement rate of 0.025 mm/s. Specimens are tested using two different clamp displacement ratios, $u_x/u_y = 1$ and $u_x/u_y = 2$. The testing protocol is briefly outlined as follows. An equi-biaxial stretch ($u_x/u_y = 1$) to a maximum clamp displacement of 3 mm is first performed. The clamps are returned to their original position and a rest period of 120 s is allowed before an non-equi-biaxial test ($u_x/u_y = 2$) is performed where $u_x^{\max} = 3$ mm. For each specimen, this procedure is repeated five times.

Inverse FE Analysis for Calibration of Anisotropic Fibres

Data collected from biaxial tests together with the shear and bulk modulus of the matrix (determined using

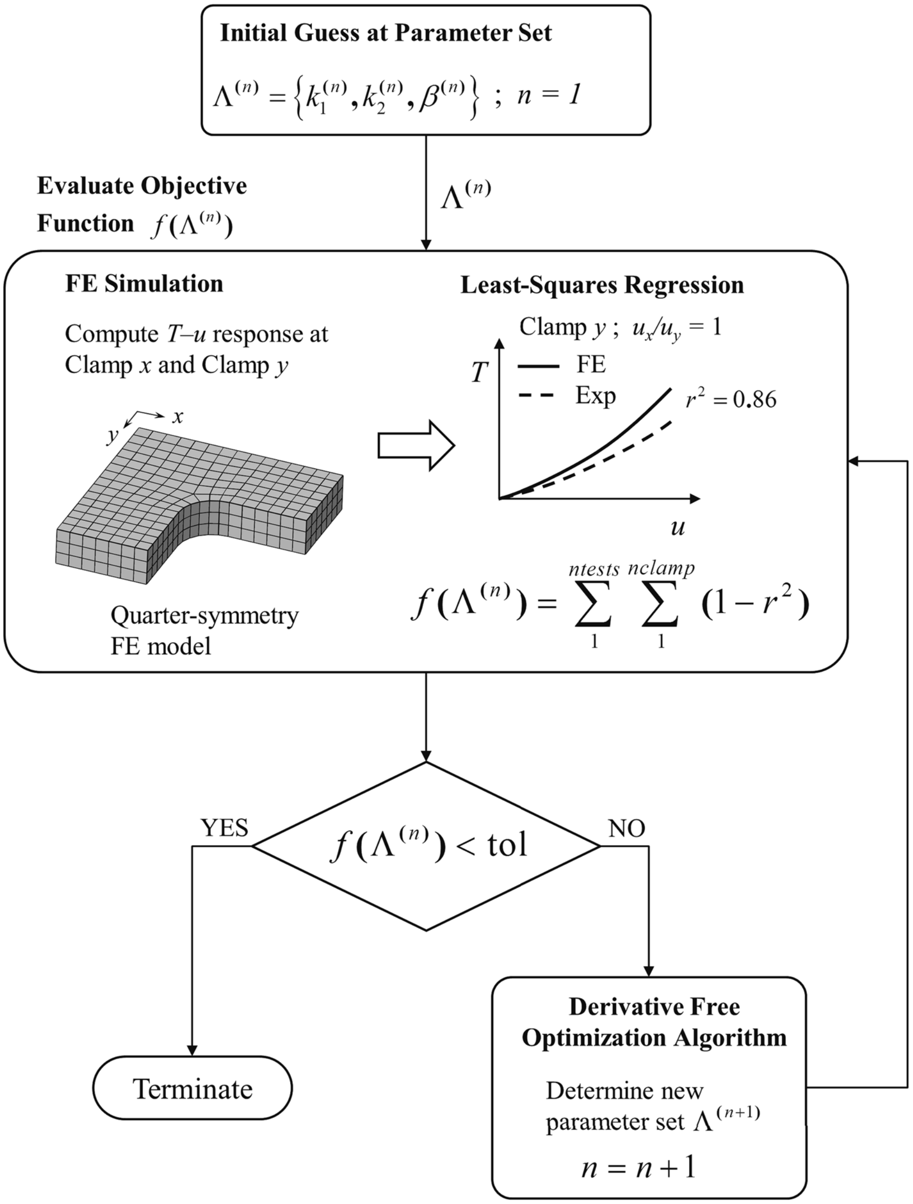

FIGURE 3. **Flowchart outlining the iterative inverse FE method used to determine material properties. An initial guess of the material properties is made for the first iteration ($n = 1$). Using this set of parameters, the objective function is evaluated. This is a two step process, firstly for each displacement ratio examined, an equivalent FE simulation is performed using the parameters defined in $\Lambda^{(n)}$. The net force–displacement (F–u) curves at each of the clamps are computed. Secondly, the FE computed force–displacement curves at each clamp for each displacement ratio are compared to their experimental counterpart using a least-squares regression method. The objective function is calculated by summing the r^2 values for each of the performed regressions. Here *ntests* is the number of displacement ratios examined and in this case is 2, *naxes* are the number of clamp force–displacement data sets and in this case is also 2 (x and y clamps). The objective function is then checked for convergence by comparing it to a tolerance set by the user. If the optimization has converged then the process is terminated. If it has not converged, the value of $f(\Lambda^{(n)})$ is returned to the optimization algorithm and a new set of material parameters $\Lambda^{(n+1)}$ is created. The process is then repeated; the objective function is evaluated and checked for convergence with new material parameters being set each time until convergence is achieved.**

the methodology described in the “Compressibility of Arterial Tissue” section) are used to calibrate the model parameters in the anisotropic terms of Eq. (1). The biaxial tests yield four independent sets of force–displacement data, one for each material axis for a given clamp displacement ratio. For a complete calibration, each material constant requires an independent data set . In the case of the MA constitutive model three material constants must be calibrated, k_1, k_2, β. The biaxial tests provide sufficient data for calibration and an additional data set for verification. The relationship between the experimentally measured force and the material stress in a biaxial test is complex. Recently Nolan and McGarry[27] demonstrated that the stress distribution in a cruciform specimen subjected to a biaxial stretch is highly non-uniform and cannot be trivially related to the measured force. Therefore an inverse FE scheme based on the force–displacement experimental data must be employed to accurately characterise the material behaviour.

Figure 3 shows a flowchart describing the inverse FE method. This entails an optimization/minimization problem where a trial set of parameters Λ are initially created and evaluated by an objective function $f(\Lambda)$. If $f(\Lambda)$ meets the convergence criteria then the process is terminated, if not then a new set of parameters are created by the optimization algorithm and the process is repeated. Specifically the set of parameters we wish to determine are the anisotropic material constants for the compressible MA constitutive model from Eq. (1); i.e. $\Lambda = \{k_1, k_2, \beta\}$. The objective function consists of two parts. The first part is the FE simulation of the biaxial tests, replicating the geometry and boundary conditions of the experiments. Simulations are performed for the displacement ratios $u_x/u_y = 1$ and $u_x/u_y = 2$. For each simulation, net force–displacement curves at the x and y clamps are computed. The second part quantifies how closely the FE simulation reproduces the experimental data. A least-squares regression is calculated comparing the experimental and FE force–displacement curves. The correlation coefficient r^2 is computed for the four sets of force–displacement data. As the correlation improves $r^2 \rightarrow 1$; $(1 - r^2)$ quantifies the goodness of fit. The objective function then is the sum of the goodness of fit measures, for the n^{th} iteration,

$$f(\Lambda^{(n)}) = \sum_{1}^{nratio} \sum_{1}^{naxes} (1 - r^2), \tag{4}$$

where *nratio* are the number of unique displacement ratios used in the biaxial testing and *naxes* are the number of axes the material is tested in. In the current study $nratio = 2$ and $naxes = 2$. Convergence is judged to have occurred when the change in $f(\Lambda)$ is less than a predefined tolerance value. If convergence does not occur, a derivative-free, Nelder–Mead simplex algorithm[23,26] is used to determine the next parameter set $\Lambda^{(n+1)}$ that should be evaluated by the objective function.

RESULTS

Compressibility of Arterial Tissue and Isotropic Ground Matrix Calibration

To assess whether any specimen damage, debonding, or plasticity occurs during the test protocol described in the "Tensile Tests" section, successive loading cycles are analysed. In all cases the measured force-deformation curves are identical for successive cycles, indicating that only elastic deformation of the specimens occurs, as expected, with the bond between the specimen and the loading platens remaining fully intact throughout (also confirmed by post-test examination). The measured force when the specimen is fully stretched is (±SD) is 0.59 ± 0.21 N ($n = 13$). Using the method outlined in the "Volume Change Measurement" section the specimen volume change following load application is determined. Figure 4 shows a bar chart of the percentage volume change in each of the specimens tested ($n = 13$); the mean percentage volume change (±SD) is $9.31 \pm 3.19\%$. Note that a volume change is determined in all cases, demonstrating that the assumption of material incompressibility is not appropriate for arterial tissue.

Finite element simulations confirm that fibres shorten under the applied mode of loading, so that experimental data can provide an independent calibration of the isotropic matrix parameters κ and μ. An inverse FE study is performed to determine the parameter values that result in the experimentally observed percentage volume change of 9.31% for an applied force of 0.59 N. Results are shown in Table 1.

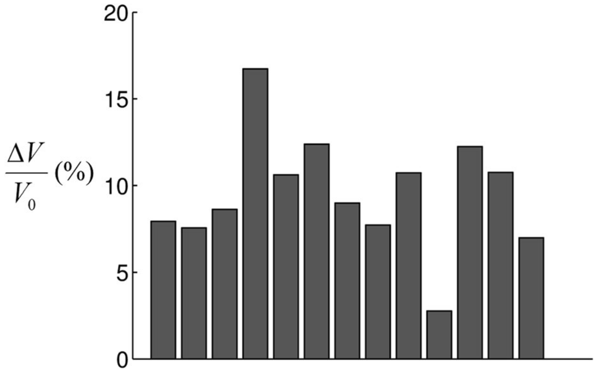

FIGURE 4. Barchart indicating the percentage volume change measured in each of the specimens tested. The mean value for the volume change (±SD) is $9.31 \pm 3.19\%$. All specimens exhibit volume change and hence should be regarded as compressible.

TABLE 1. Table of the material properties κ and μ computed from the inverse FE scheme outlined in Fig. 1c using the mean value of force measured in the experiments and ± one standard deviation as the upper and lower bounds.

	$\Delta V/V_0$ (%)	μ (kPa)	κ (kPa)	κ/μ	ν_{eff}
Upper	12.50	7.87	42.14	5.34	0.412
Mean	9.31	6.47	56.66	8.56	0.445
Lower	6.12	6.25	99.03	15.79	0.469

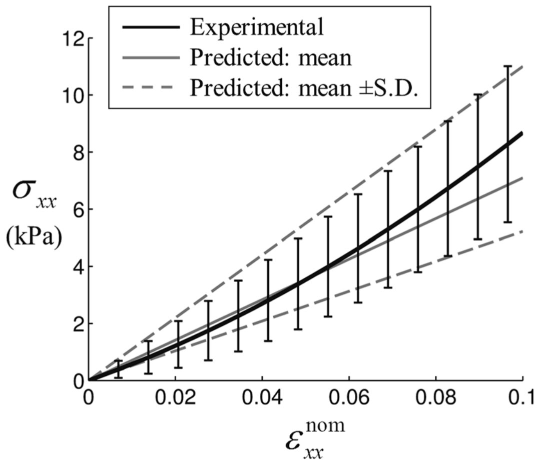

FIGURE 5. Stress–strain curve for confined compression tests (n = 9). Also shown is the predicted stress–strain behaviour, based on a neo–Hookean constitutive law and the compressible material parameters determined from the tensile tests (Table 1). Note that the axial strain $\varepsilon_{xx}^{\text{nom}}$ is equal to the volumetric strain $\Delta V/V_0$ in confined compression.

TABLE 2. Results from the inverse FE scheme for the anisotropic material parameters of the MA model defined in Eq. (1).

k_1 (kPa)	k_2	β (°)	$r^2 \geq$	$f(\Lambda)$
4.81	1.98	60.2	0.97	0.07

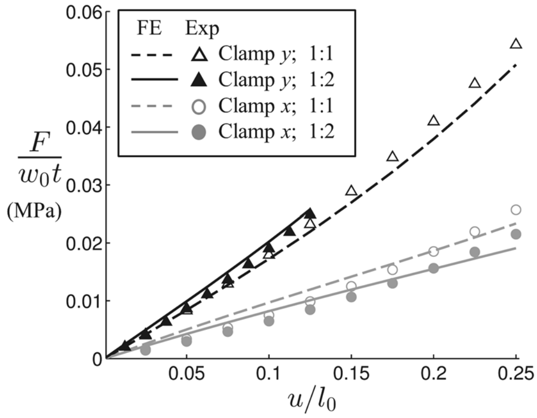

FIGURE 6. Calibration of the biaxial tests using the compressible MA model. (a) Force–displacement curves for clamps x and y and displacement ratios $u_x/u_y = 1$ and $u_x/u_y = 2$. The solid lines are the experimentally measured curves whilst the symbols represent the best fit FE solution. The cost function for this calibration is $f(\Lambda) = 0.072$ while the lowest value of the correlation coefficient $r^2 = 0.97$. Material parameters are give in Table 2.

For completeness, calibrations are also performed using target experimental values one standard deviation above and below the mean values, providing upper and lower limits for the material constants. As reported in Table 1, using (3), the effective Poisson's ratio of the arterial tissue ranges from 0.412 to 0.469, again indicating that the material is indeed compressible.

Confined Compression Test Results

Figure 5 shows the experimental axial stress–strain curve for the confined compression test (mean ± SD). Also shown is the predicted stress–strain curve using the compressible neo–Hookean material parameters determined from the aforementioned tension tests (mean, upper and lower bounds given in Table 1). The experimental and predicted confined compression data are in good agreement with one another. This result provides a validation of the material parameters for the compressible ground matrix determined in above. It should be noted that the axial strain $\varepsilon_{xx}^{\text{nom}}$ is equal to the volumetric strain $\Delta V/V_0$ in this confined compression experiment.

Anisotropic Material Constant Calibration

The anisotropic material properties k_1, k_2 and β for the MA constitutive model given in Eq. (1) are determined from biaxial tension experiments using the method outlined in the "Inverse FE Analysis for Calibration of Anisotropic Fibres" section. The mean force–displacement curve ($n = 6$) is used as the target experimental data and a mean specimen thickness of 2.9 mm is assigned to the FE model. Table 2 gives the material properties determined from this analysis and Fig. 6a plots normalized force–displacement curves in the x and y directions for biaxial displacement ratios of $u_x/u_y = 1$ and $u_x/u_y = 2$. A good correlation between the measured experimental data and calibrated FE simulations is achieved ($r^2 > 0.97$ for all plots). As expected, highly anisotropic material behaviour is observed, with the measured force being significantly higher in the circumferential direction of the sample. It should also be noted that force–displacement curves are quite linear, with no significant strain stiffening being observed over the range of applied deformation (the maximum principal nominal strain at the centre of the specimen $\varepsilon_{\text{nom}}^{\text{maxp}} = 25\%$ at maximum extension).

Additionally in Appendix B we perform specimen-specific calibrations of each biaxial test, where the unique specimen thickness and force–displacement curves are used.

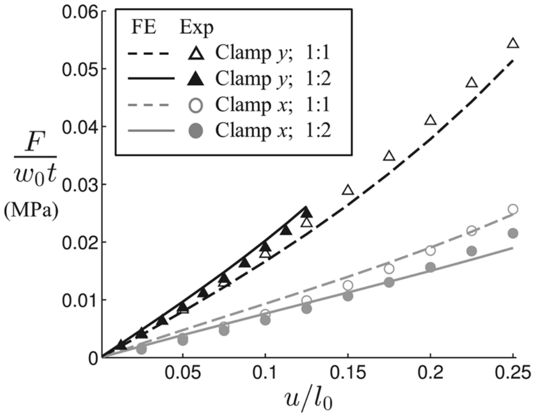

FIGURE 7. Calibration of the biaxial tests using the incompressible HGO model. (a) Mean force–displacement curves for clamps x and y and displacement ratios $u_x/u_y = 1$ and $u_x/u_y = 2$. The solid lines are the experimentally measured curves whilst the symbols represent the best fit FE solution. The cost function for this calibration is $f(\Lambda) = 0.071$ while the lowest value of the correlation coefficient $r^2 = 0.97$.

Assessment of Error Generated by the Incompressibility Assumption

Having established that aorta arterial tissue is compressible, we next assess the errors introduced by the commonly used assumption of material incompressibility. Assuming that the material is incompressible, a ground matrix shear modulus is calibrated using the method outlined in the "Calibration of Isotropic Ground Matrix" section while ignoring the experimentally measured volume change reported in Table 1. A shear modulus of $\hat{\mu} = 5.2$ kPa is found to reproduce the experimentally measured mean applied force of 0.59 N at $\lambda_{\text{nom}} = 1.28$ nominal stretch ratio (see Fig. 1), but with no volume change permitted. Next the anisotropic material parameters for the incompressible HGO model[19] are calibrated from the biaxial test data using the inverse FE procedure outlined in the "Inverse FE Analysis for Calibration of Anisotropic Fibres" section. Anisotropic material constants of $\hat{k}_1 = 6.92$ kPa, $\hat{k}_2 = 0.89$ and $\hat{\beta} = 57.5°$ are determined (see Fig. 7).

In Fig. 7 it appears that a very accurate calibration of the material properties has been achieved using the incompressible HGO model ($r^2 > 0.97$). However, noting that this calibration has been performed while ignoring the previously determined material compressibility, we next demonstrate that significant errors may be encountered by the inaccurate incompressibility assumption in a tri-axial loading environment. Specifically we consider the case of an artery expansion under increasing lumen pressure using both the compressible MA model and the incompressible HGO model. The artery is modelled as a three-dimensional thick walled cylinder with fixed ends (no net out-of-plane deformation is permitted in the z-direction). Figure 8a illustrates the geometry and boundary conditions in addition to the applied lumen pressure LP. The artery is inflated up to a maximum lumen pressure ($LP_{\max}$) of 4.0 kPa. A mesh sensitivity study determines that 1600 elements result in a sufficiently converged solution. We ensure that the maximum principal strain in the vessel wall does not exceed the maximum strain used in calibrating the models.

Figure 8b plots the internal and external radial strain ($\Delta r/r_0$) with increasing lumen pressure (LP) for both the MA and HGO models. Both models predict near identical arterial compliance. This simulation is analogous to a 1:0 biaxial stretch in the $\theta - z$ plane with an additional small compressive stress in the radial direction. The $\sigma_{\theta\theta}$ and σ_{zz} stress components are at least two orders of magnitude greater than the σ_{rr} radial stress, highlighting that the dominant deformation occurs primarily in the plane of the fibres. Given that the MA and HGO models are calibrated to give an identical response in biaxial tension (see Figs. 6 and 7 respectively), a similar arterial compliance is computed by both models as shown in Fig. 8b.

However the calibrated MA model, which correctly accounts for compressibility, predicts a very different stress state in the artery wall to the HGO model which does not account for compressibility. Figure 8c, d demonstrate that the entire stress distribution is significantly affected. Figure 8c considers the stress biaxiality in the artery wall i.e. the ratio of the axial to circumferential stress ($\sigma_{zz}/\sigma_{\theta\theta}$). The models compute a significantly different magnitude and gradient of stress biaxiality through the artery wall. Clearly the incompressibility assumption has significant implications for the out-of-plane axial stress (σ_{zz}) component, with important consequences for prediction of artery buckling stress[15] *etc.* Figure 8d considers the stress triaxiality in the artery wall; the ratio of the pressure stress ($p = tr(\sigma)$) to the von Mises stress ($q = \sqrt{(3/2)\sigma' : \sigma'}$ where σ' is the deviatoric stress). Stress triaxiality is an indication of the volumetric to deviatoric (shear) stress at a material point and is often used as a scalar measure of a tri-axial stress state. Additionally stress trixiality has been shown to be an important factor in crack nucleation and material rupture.[1] Significant differences in stress triaxiality magnitude and gradient are computed even though both models have been accurately calibrated to biaxial test data ($r^2 > 0.97$)

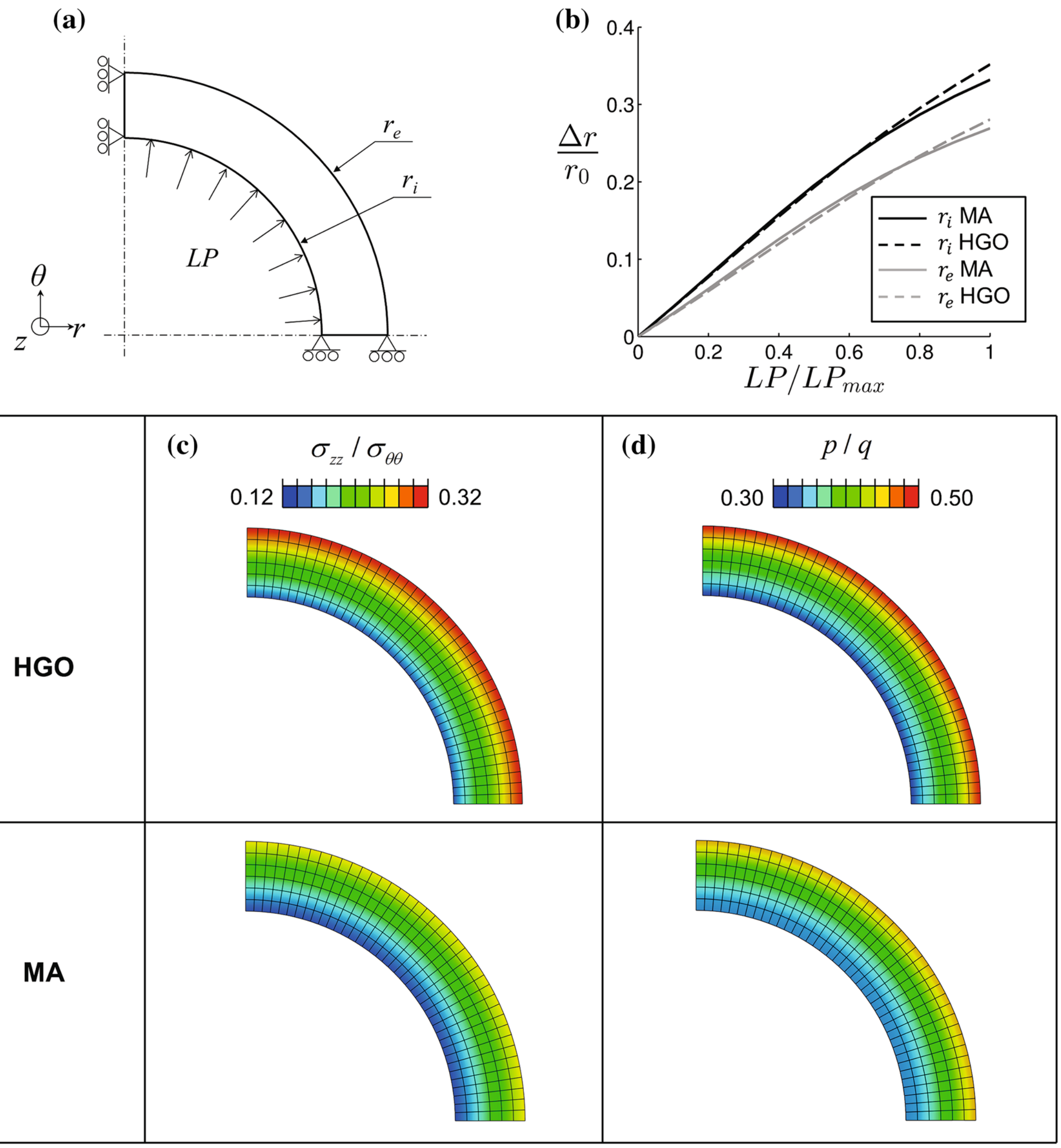

FIGURE 8. **(a) Schematic of a quarter artery showing the geometry and boundary conditions used for the FE simulations. The artery has an internal radius $r_i = 9$ mm and an external radius $r_e = 12$ mm and is subjected to an internal lumen pressure $LP_{\text{max}} = 4.0$ kPa. (b) Plot showing the predicted internal and external radial strain ($\Delta r/r_0$) with increasing lumen pressure (LP) for the compressible MA model and the incompressible HGO model. (c) Contour plot of the axial Cauchy stress σ_{zz} over the circumferential Cauchy stress $\sigma_{\theta\theta}$ (the plane in which the reinforcing fibres are located) computed by the HGO and MA models. The contour shows a marked difference in the stress distribution in the artery wall. (d) Contour plot of the stress triaxiality (p/q) in the artery wall computed by the HGO and MA model. Stress triaxiality is the pressure stress p over the von Mises stress q . Again we see marked differences in the triaxiality of the stress. Note that all contour plots are plotted in the undeformed configuration for the purposes of comparison.**

and exhibit similar material compliance. The values of q , p , σ_{zz}, and $\sigma_{\theta\theta}$ at the internal and external radius for both the HGO and MA models are given in Table 3.

Appendix D simulates lumen inflation where residual stresses in the vessel wall have been included. Results show that, once again, compressibility of the tissue has an important influence on the stress-state in the vessel wall.

DISCUSSION

The current study provides new insight into the compressibility of arterial tissue. The key findings of the study are as follows:

1. Aortic arterial tissue is compressible. Stretching of aortic tissue specimens in the radial direction reveals significant volume changes (mean $\Delta V/V_0 = 9.31\%$).

TABLE 3. Values of the von Mises stress (q), pressure stress (p), axial stress (σ_{zz}), and circumferential stress ($\sigma_{\theta\theta}$) at internal radius, r_i, and the external radius, r_e.

	MA		HGO	
	r_i	r_e	r_i	r_e
q (kPa)	32.26	11.98	30.69	13.22
p (kPa)	10.95	5.55	9.93	6.52
σ_{zz} (kPa)	4.42	3.59	4.68	4.18
$\sigma_{\theta\theta}$ (kPa)	31.96	13.24	29.81	14.97

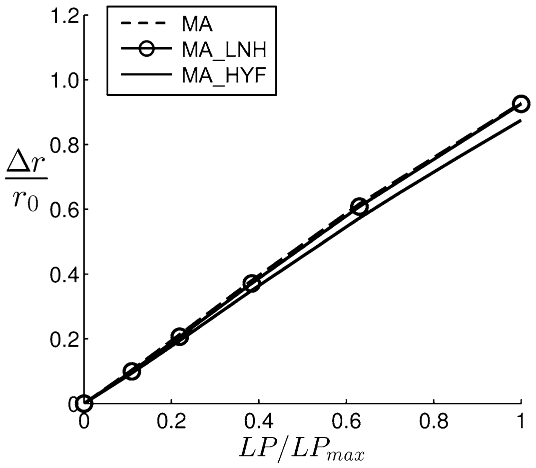

FIGURE A.1. Mean radial strain with increasing lumen pressure for (i) the MA model (Eq. (1)), (ii) the MA_LNH model which uses a modified version of the neo–Hookean model to represent the ground matrix; this version uses a logarithmic penalty term ln(J) to prevent excessive volumetric deformations, and iii) the MA_HYF model which uses a hyperfoam model to represent the ground matrix.

2. Biaxial stretch experiments alone are not sufficient to characterise tissue behaviour. We demonstrate that the incompressible HGO model and its modified compressible form (MA model) can both be accurately calibrated to capture experimental biaxial test data ($r^2 > 0.97$ for both), despite the fact the HGO model neglects material compressibility.
3. Failure to accurately characterize tissue compressibility will result in the inaccurate prediction of artery wall material stress *in vivo*, even if artery compliance is accurately calibrated.

Previously published material models assume that arterial tissue is incompressible,[5,14,19,39] as do many experimental studies.[16,21,30,32,40] The paper by Carew *et al.*[4] is generally cited as justification for the assumption of incompressibility. Carew *et al.*[4] expanded segments of artery under physiological lumen pressure and the change in volume of the artery tissue was measured. No significant volume change was observed but critically the study is limited to the small strain regime. Moreover the study of DiPuccio *et al.*[8] suggests that accuracy of the technique used by Carew *et al.* should be improved upon. Previous studies have attempted to measure volume change by directly measuring artery geometry.[2,9] During lumen expansion the change in vessel thickness scales with the square root of the volume change. Hence in a lumen expansion experiment, the measurement of volume change *via* the change in internal and external radii requires very accurate measurement and presents a considerable experimental challenge.

In the current study a novel combined experimental and computational approach is developed to overcome this challenge. By stretching aortic arterial tissue in the radial direction and monitoring resultant changes in the tissue volume, it is shown that aortic ground matrix material exhibits significant compressibility. This methodology for the determination of tissue compressibility is based on experimental evidence that fibres are primarily confined to the $\theta - z$ plane[12] and hence do not contribute to stretching in the radial direction. A number of papers report dispersion of the fibre orientation angles in arteries.[3,13] This may lead to a small contribution of fibres in the radial direction but it is expected that this is a secondary effect as it is generally accepted that arteries have two families of fibres in the $\theta - z$ plane.[19,34] This novel technique allows the determination of material compressibility, while parsing isotropic contribution of the ground matrix. To further validate this finding, we perform additional experimental tests for a confined compression mode of deformation; confined compression results are in close agreement with our tension tests.

In addition to stretching in the radial direction, biaxial tests are performed to determine fibre mechanical properties. An inverse FE method is used to provide an optimal calibration of the fibre properties from the experimental results. In the current study we demonstrate that if material compressibility is not independently established, a unique set of anisotropic material properties cannot be determined through biaxial tests alone. To highlight this point we demonstrate that biaxial experimental test data can be accurately predicted by both the compressible MA material model ($r^2 > 0.97$) and the incompressible HGO material model ($r^2 > 0.97$). This is despite the fact that the aforementioned compressibility was rigorously established in the "Compressibility of Arterial Tissue" section. The parsing of the matrix contribution using the method in the "Compressibility of Arterial Tissue" section and determination of fibre properties as shown in the "Biaxial Experiments" section provides a new and systematic approach to the mechanical characterisation of soft tissue.

In the current study aorta tissue exhibits slightly non-linear stress–strain behaviour in the strain range examined ($\varepsilon_{\mathrm{nom}}^{\mathrm{maxp}} = 25\%$ at the specimen centre at maximum extension). Such near-linear behaviour is similar to the uniaxial experimental results of Sokolis *et al.*[37] In contrast highly non-linear exponential strain stiffening has been observed for coronary and carotid arteries for strain ranges up to 30%.[22,35] Future studies should investigate changes in material compressibility at very high levels of applied strain (both compressive and tensile).

The current study is the first to present rigorous quantification of aorta compressibility. Follow-on studies should be performed on other types of elastic arteries e.g. carotid, iliac arteries, as well as muscular arteries, e.g. femoral, cerebral arteries, in order to characterise ground matrix compressibility as a function of anatomical location. Given the similarities in anatomical composition of all elastic arteries,[22] based on the current study it is not unreasonable to suggest that they will exhibit some degree of compressibility. Future studies should also consider both healthy and diseased human arterial tissue. It is possible that the level of compressibility aneurysmal tissue or atherosclerotic tissue may differ from that of healthy tissue. The recent study by Yosibash *et al.*[46] reports volume changes in segments of porcine femoral and saphenous arteries under lumen pressure however precise characterisation of material compressibility has yet to be performed.

The significant errors that can result from an inappropriate incompressibility assumption are highlighted in the case study of a 3D artery subjected to a lumen pressure. In this case study the artery is subjected to a triaxial stress state hence exposing the significant errors that can be generated if material compressibility is not properly characterised. Though a change in volume of the artery wall is computed using the compressible MA model, because the change in artery wall thickness scales approximately with the square root of the volume change, a small change in artery wall volume (≈2%) results in a very small change in vessel radius.

The importance of compressibility on the biaxial and triaxial stress reported in this study is not surprising, based on theoretical analysis that demonstrates that stresses in thick walled elastic cylinders are dependent on compressibility.[25] The importance of compressibility has also been demonstrated in cases where residual stress has been included. The theoretical relationship between residual stress and compressibility was previously noted.[44]

TABLE B.1. Anisotropic material parameters for the MA model defined in Eq. (1) uniquely calibrated for each individual specimen, as well as the individual specimen thickness.

	#1	#2	#3	#4	#5	#6
t (mm)	3.5	3.3	2.8	2.4	2.9	2.7
k_1 (kPa)	11.91	6.73	6.49	7.84	8.92	5.59
k_2	0.5	0.5	0.5	0.5	0.5	0.5
β (°)	57.7	54.9	62.0	59.3	59.5	62.8
r^2	0.98	0.97	0.97	0.95	0.98	0.93
$f(\Lambda)$	0.056	0.129	0.061	0.146	0.050	0.175

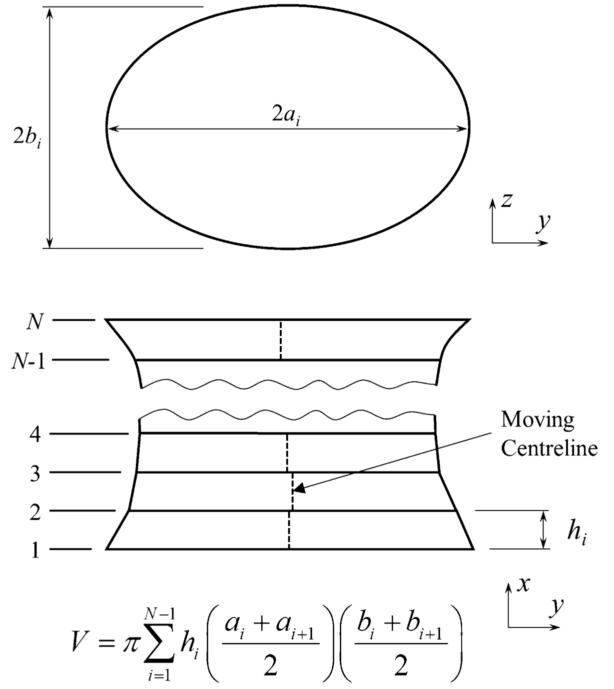

$$V = \pi \sum_{i=1}^{N-1} h_i \left(\frac{a_i + a_{i+1}}{2}\right)\left(\frac{b_i + b_{i+1}}{2}\right)$$

FIGURE C.1. Quasi-3D calculation to determine the volume change in cylindrical specimens. Orthogonal experimental images measure the orthogonal diameters, 2*a* and 2*b*, of the specimen at each segmentation plane. The volume, *V* , is calculated by integrating cross-sectional areas over the height of the specimen.

These alterations have important consequences for all manner of biomechanics and medical device simulations. Correct modelling of vessel compliance and stress are vital for the accurate simulation of many biomechanics and medical device problems. For example; the radial force required to deploy a stent, stent recoil and fatigue,[7] for peripheral vessel buckling and deformation,[15] and for prediction of abdominal aortic aneurysm rupture.[45]

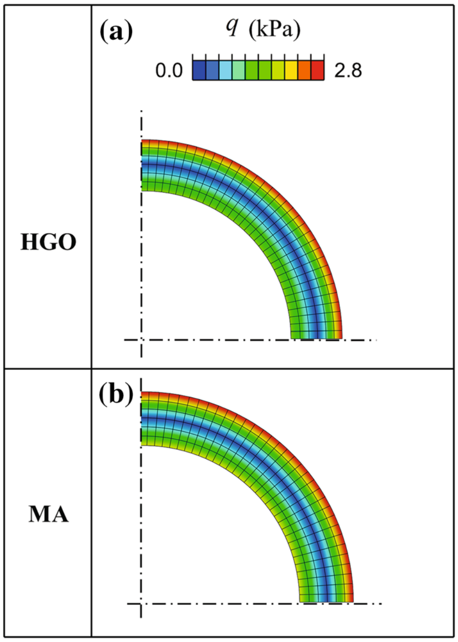

FIGURE D.1. Residual (von Mises) stress in the vessel wall under zero lumen pressure for (a) the incompressible HGO model, and (b) the compressible MA model.

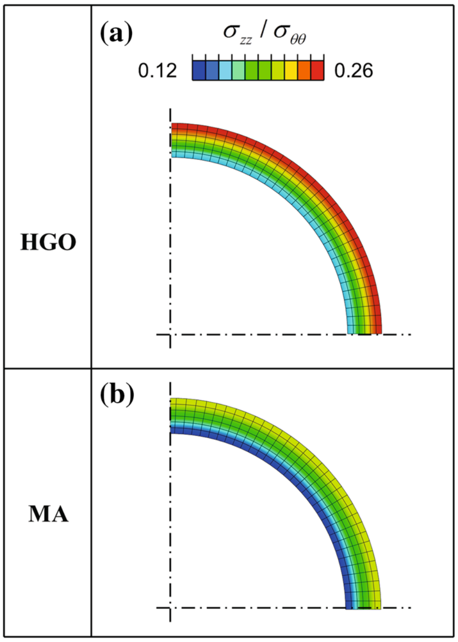

FIGURE D.2. Ratio of the axial stress to the circumferential stress ($\sigma_{zz}/\sigma_{\theta\theta}$) in a pressurized vessel for (a) the incompressible HGO model, and (b) the compressible MA model. Results are similar to those presented in Fig. 8

CONCLUSION

In the current paper we have determined that aortic arterial tissue is compressible. A rigorous methodology for calibration of the isotropic ground matrix and anisotropic fibre contribution is presented. Finally we demonstrate that material compressibility must be accounted for in order to accurately predict the stress state of an artery wall.

APPENDIX A: INVESTIGATION OF DIFFERENT FORMS OF Ψ_{iso}

In the "Compressible Anisotropic Constitutive Model" section the strain energy potential for the MA model is additively split into isotropic and anisotropic parts $\Psi = \Psi_{\mathrm{iso}} + \Psi_{\mathrm{aniso}}$. The MA model uses a common neo–Hookean strain energy potential, $\Psi_{\mathrm{iso}} = \frac{\mu}{2}(\bar{I}_1 - 3) + \frac{\kappa}{2}(J-1)^2$. Here the use of two additional hyperelastic strain energy potentials for use as the isotropic term Ψ_{iso} are investigated. Firstly a modified version of the standard neo–Hookean model which was developed for scenarios involving large compressive stresses is examined. Its strain energy potential is given as:

$$\Psi_{\mathrm{iso}} = \frac{\mu}{2}(\bar{I}_1 - 3) + \frac{\kappa}{2}\left(\frac{J^2 - 1}{2} - \ln(J)\right). \tag{A.1}$$

In this model the volumetric term has been modified to include the function $\ln(J)$. This has the effect of penalising very large volume changes and prevents $J \to 0$.

Secondly a hyperfoam model[38] developed for highly compressible hyperelastic polymer foams is examined. Its strain energy function is given as:

$$\Psi_{\mathrm{iso}} = \sum_{i=1}^{N} \frac{2\mu_i}{\alpha_i^2}\left[\lambda_1^{\alpha_i} + \lambda_2^{\alpha_i} + \lambda_3^{\alpha_i} - 3 + \frac{1}{\beta_i}\left(J^{-\alpha_i \beta_i} - 1\right)\right], \tag{A.2}$$

where N is the order of the function, λ_m $(m = 1, 2, 3)$ are the principal stretches, α_i determines the non-linearity for each term in the function, β_i determines the compressiblity for each term in the strain energy function and is related to the Poisson's ratio v_i through the expression $\beta_i = v_i/(1 - 2v_i)$, and the initial bulk modulus $\kappa_0 = \sum_{i=1}^{N} 2\mu_i[(1 - 3\beta_i)/3]$.

Equation (A.1) is added to the anisotropic potential of the MA model to form the MA_LNH model and Eq. (A.2) is added to the anisotropic potential of the MA model to form the MA_HYF model. The simulations from "Assessment of Error Generated by the Incompressibility Assumption" are repeated using the MA_LNH and MA_HYF models for the artery wall. The MA_LNH model uses the mean bulk and shear modulus from Table 1 and the MA_HYF model uses $N = 1$, $\alpha_i = 2$, $v_i = 0.44$, and $\mu_i = 7.04$ kPa.

The mean radial strain – pressure curves for both of these models, as well as that of the original MA model are given in Fig. A.1. Use of the MA_LNH model results in no difference in arterial compliance compared to the MA model. The MA_HYF model computes a small difference in compliance. For the hyperfoam model it is recommended that the effective Poisson’s ratio does not exceed 0.45.

APPENDIX B: CALIBRATION OF ANISOTROPIC CONSTITUTIVE MODELS

Calibrations are performed for each of the six individual specimens tested using their unique force–displacement curve and the specimen thickness measured using the technique outlined in “Inverse FE Analysis for Calibration of Anisotropic Fibres” section. The results of these individual calibrations are presented in Table B.1.

APPENDIX C: QUASI-3D METHOD FOR VOLUME CHANGE MEASUREMENT

Volume change is calculated using an alternative method by measuring two orthogonal axes/diameters of the specimen at each segmentation plane. The volume is computed by integrating the resultant cross-sectional areas over the height of the specimen using a trapezoidal type method. A schematic outlining this method is given in Fig. C.1 This alternative methodology results in a volume change of 10.11 ± 4.61% (mean ± SD). A t test indicates that there is no statistically significant difference between the mean volume change calculated using the axi-symmetric or the quasi-3D method.

APPENDIX D: INCLUSION OF RESIDUAL STRESS

The influence of residual stresses on the stress-state in the vessel wall is assessed in this appendix. It is well established that residual stresses are present in the unpressurised vessel wall. Simulations of lumen inflation were performed, following the computational method outlined by Raghavan *et al.*[31] and using the experimental data of Vaishnav and Vossoughi[42] to determine stress-free geometry. The vessel has a stress-free internal radius $R_i = 21.92$ mm, an external radius $R_e = 24.94$ mm, and an opening angle of 80.22°. The material parameters for both the HGO and MA models are identical to those used in “Assessment of Error Generated by the Incompressibility Assumption” section.

Figure D.1 shows a contour plot of the residual von Mises stress in the vessel wall in the unpressurised configuration. The vessel moves from a state of compression on the inner face to tension on the external face. As the anisotropic component of both the HGO and MA models are inactive in compression, this explains the higher stress on the external face of the vessel. Figure D.2 shows a contour plot of the ratio of the axial stress to the circumferential stress ($\sigma_{zz}/\sigma_{\theta\theta}$) for the HGO and MA models. This figure further illustrates the dependence of the stress-state on the treatment of compressibility. Differences between the HGO and MA models are similar to those shown in Fig. 8 without residual stress. This illustrates that the important influence of compressibility on triaxial artery stress is significant regardless of the inclusion of residual stress.

ACKNOWLEDGMENTS

The authors wish to acknowledge funding from Science Foundation Ireland under project SFI-12/IP/1723. Furthermore we acknowledge funding from the Irish Research Council and the College of Engineering and Informatics at NUI, Galway. The authors wish to thank Noel Reynods and Prof. Michel Destrade for insightful discussions on this topic.

REFERENCES

[1] Anderson, T. L. Fracture mechanics: fundamentals and applications. Boca Raton: CRC press, 2005.

[2] Boutouyrie, P., D. P. Germain, A.-I. Tropeano, B. Laloux, F. Carenzi, M. Zidi, X. Jeunemaitre, and S. Laurent. Compressibility of the carotid artery in patients with pseudoxanthoma elasticum. *Hypertension*. 38:1181–1184, 2001.

[3] Canham, P. B., H. M. Finlay, J. G. Dixon, D. R. Boughner, and A. Chen. Measurements from light and polarised light microscopy of human coronary arteries fixed at distending pressure. *Cardiovasc. Res*. 23:973–982, 1989.

[4] Carew, T. E., R. N. Vaishnav, and D. J. Patel. Compressibility of the arterial wall. *Circ. Res*. 23:61–68, 1968.

[5] Chuong, C., and Y. Fung. Three-dimensional stress distribution in arteries. *J. Biomech. Eng*. 105:268–274, 1983.

[6] Chuong, C., and Y. Fung. Compressibility and constitutive equation of arterial wall in radial compression experiments. *J. Biomech*. 17:35–40, 1984.

[7] Conway, C., F. Sharif, J. McGarry, and P. McHugh. A computational test-bed to assess coronary stent implantation mechanics using a population-specific approach. *Cardiovasc. Eng. Technol*. 3:374–387, 2012.

[8] Di Puccio, F., S. Celi, and P. Forte. Review of experimental investigations on compressibility of arteries and

introduction of a new apparatus. *Exp. Mech.* 52:895–902, 2012.

[9] Dobrin, P., and A. Rovick. Static elastic properties of dog carotid arterial wall. *Fed. Proc.* 26:439, 1967.

[10] Dobrin, P. B. Biaxial anisotropy of dog carotid artery: estimation of circumferential elastic modulus. *J. Biomech.* 19:351–358, 1986.

[11] Elliott, D. M., and L. A. Setton. Anisotropic and inhomogeneous tensile behavior of the human anulus fibrosus: experimental measurement and material model predictions. *J. Biomech. Eng.* 123:256–263, 2001.

[12] Finlay, H., L. McCullough, and P. Canham. Three-dimensional collagen organization of human brain arteries at different transmural pressures. *J. Vasc. Res.* 32:301–312, 1995.

[13] Finlay, H. M., P. Whittaker, and P. B. Canham. Collagen organization in the branching region of human brain arteries. *Stroke* 29: 1595–1601, 1998.

[14] Gasser, T. C., R. W. Ogden, and G. A. Holzapfel. Hyperelastic modelling of arterial layers with distributed collagen fibre orientations. *J. R. Soc. Interface* 3:15–35, 2006.

[15] Ghriallais, R. N., and M. Bruzzi. Effects of knee flexion on the femoropopliteal artery: a computational study. *Med. Eng. Phys.* 35: 1620–1628, 2013.

[16] Hayashi, K., H. Handa, S. Nagasawa, A. Okumura, and K. Moritake. Stiffness and elastic behavior of human intracranial and extracranial arteries, *J. Biomech.* 13:175–184, 1980.

[17] Holzapfel, G. A. Nonlinear solid mechanics: a continuum approach for engineers. Wiley: Chichester, 2000.

[18] Holzapfel, G. A., and R. W. Ogden. On planar biaxial tests for anisotropic nonlinearly elastic solids. A continuum mechanical framework. *Math. Mech. Solids* 14:474–489, 2009.

[19] Holzapfel, G. A., T. C. Gasser, and R. W. Ogden. A new constitutive framework for arterial wall mechanics and a comparative study of material models. *J. Elast. Phys. Sci. Solids* 61:1–48, 2000.

[20] Huang, C.-Y., A. Stankiewicz, G. A. Ateshian, and V. C. Mow. Anisotropy, inhomogeneity, and tension–compression nonlinearity of human glenohumeral cartilage in finite deformation. *J. Biomech.* 38:799–809, 2005.

[21] Humphrey, J., D. Vawter, and R. Vito. Pseudoelasticity of excised visceral pleura. *J. Biomech. Eng.* 109:115–120, 1987.

[22] Humphrey, J. D. Cardiovascular solid mechanics: cells, tissues, and organs. Springer: New York, 2002.

[23] Lagarias, J., J. Reeds, M. Wright, and P. Wright. Convergence properties of the nelder–mead simplex method in low dimensions. *SIAM J. Optim.* 9:112–147, 1998.

[24] Lawton, R. W. The thermoelastic behavior of isolated aortic strips of the dog. *Circ. Res.* 2:344–353, 1954.

[25] Misra, J., and S. Chakravarty. Study of compressibility in vascular rheology. *Rheol. Acta* 19:381–388, 1980.

[26] Nelder, J. A., and R. Mead. A simplex method for function minimization. *Comput. J.* 7:308–313, 1965.

[27] Nolan, D., and J. McGarry. On the correct interpretation of measured force and calculation of material stress in biaxial tests. *J. Mech. Behav. Biomed. Mater.* 2015. doi: 10.1016/j.jmbbm.2015.08.019.

[28] Nolan, D., A. Gower, M. Destrade, R. Ogden, and J. McGarry. A robust anisotropic hyperelastic formulation for the modelling of soft tissue. *J. Mech. Behav. Biomed. Mater.* 39:48–60, 2014.

[29] Peña, E., A. P. Del Palomar, B. Calvo, M. Martínez, and M. Doblaré. Computational modelling of diarthrodial joints. physiological, pathological and pos-surgery simulations. *Arch. Comput. Methods Eng.* 14:47–91, 2007.

[30] Raghavan, M., and D. A. Vorp. Toward a biomechanical tool to evaluate rupture potential of abdominal aortic aneurysm: identification of a finite strain constitutive model and evaluation of its applicability. *J. Biomech.* 33:475–482, 2000.

[31] Raghavan, M., S. Trivedi, A. Nagaraj, D. McPherson, and K. Chandran. Three-dimensional finite element analysis of residual stress in arteries. *Ann. Biomed. Eng.*, 32, 257–263, 2004.

[32] Sacks, M. S. Biaxial mechanical evaluation of planar biological materials. *J. Elast. Phys. Sci. Solids* 61:199–246, 2000.

[33] Schneider, C. A., W. S. Rasband, and K. W. Eliceiri. NIH image to ImageJ: 25 years of image analysis. *Nat. Methods* 9:671–675, 2012.

[34] Silver, F., D. Christiansen, and C. Buntin. Mechanical properties of the aorta: a review. *Crit. Rev. Biomed. Eng.* 17:323–358, 1988.

[35] Silver, F. H., P. B. Snowhill, and D. J. Foran. Mechanical behavior of vessel wall: a comparative study of aorta, vena cava, and carotid artery. *Ann. Biomed. Eng.* 31:793–803, 2003.

[36] Smith, H. E., T. J. Mosher, B. J. Dardzinski, B. G. Collins, C. M. Collins, Q. X. Yang, V. J. Schmithorst, and M. B. Smith. Spatial variation in cartilage t2 of the knee. *J. Magn. Reson. Imaging* 14:50–55, 2001.

[37] Sokolis, D. P., E. M. Kefaloyannis, M. Kouloukoussa, E. Marinos, H. Boudoulas, and P. E. Karayannacos. A structural basis for the aortic stress–strain relation in uniaxial tension. *J. Biomech.* 39:1651–1662, 2006.

[38] Storåkers, B. On material representation and constitutive branching in finite compressible elasticity. *J. Mech. Phys. Solids* 34:125–145, 1986.

[39] Sun, W., and M. S. Sacks. Finite element implementation of a generalized fung-elastic constitutive model for planar soft tissues. *Biomech. Model. Mechanobiol.* 4:190–199, 2005.

[40] Takamizawa, K., and K. Hayashi. Strain energy density function and uniform strain hypothesis for arterial mechanics. *J. Biomech.* 20:7–17, 1987.

[41] Tickner, E. G., and A. H. Sacks. A theory for the static elastic behavior of blood vessels. *Biorheology* 4:151, 1967.

[42] Vaishnav, R. N., and J. Vossoughi. Residual stress and strain in aortic segments. *J. Biomech.* 20:235–239, 1987.

[43] Vilarta, R., and B. D. C. Vidal. Anisotropic and biomechanical properties of tendons modified by exercise and denervation: aggregation and macromolecular order in collagen bundles. *Matrix* 9:55–61, 1989.

[44] Volokh, K. Compressibility of arterial wall in ring-cutting experiments. *Mol. Cell. Biomech.* 3:35, 2006.

[45] Vorp, D. A., M. Raghavan, and M. W. Webster. Mechanical wall stress in abdominal aortic aneurysm: influence of diameter and asymmetry. *J. Vasc. Surg.* 27:632–639, 1998.

[46] Yosibash, Z., I. Manor, I. Gilad, and U. Willentz. Experimental evidence of the compressibility of arteries. *J. Mech. Behav. Biomed. Mater.* 39:339–354, 2014.